Supporting Information

Amini et al. 10.1073/pnas.1207550109

SI Text

Inertial Focusing of Particles and the Required Channel Length. In regards to the behavior of the particle itself, with a combination of confinement and inertia, it has been shown that a particle flowing downstream migrates across streamlines and focuses to a lateral dynamic equilibrium position that corresponds to channel symmetry (1). This inertial focusing is due to a balance between (i) a wall effect lift force, which acts to drive the particle towards the channel center, and (ii) inertial lift due to the shear gradient present in a Poiseuille flow that tends to drive the particle towards the channel wall. As a consequence, particles flowing in rectangular channels will focus to positions about halfway between the center and wall of the channel (1). It is worth noting that at large H/a ($> \sim 10$) particles are able to form trains at multiple locations across the channel (2, 3). However, for the rectangular channels that we make use of here, particles normally focus to two streamlines centered on the long faces of the channel (4), which is further decreased to one focusing position by introducing particles from only one of the two inlets (5). An expression that gives the length required for particles to reach their focusing position (L_f) has been proposed that depends on fluid properties, flow velocity, particle size, and channel geometry (6). For a flow containing 10 μm particles in a 40×60 μm channel at 100 μL/min, L_f is on the order of a few millimeters. Therefore, in a channel exceeding this length, we can assume that particles stably translate downstream at focusing positions, experiencing a steady rotational motion due to the velocity differences across them.

Microfabrication. Microfluidic devices were fabricated using polydimethylsiloxane (PDMS) replica molding processes. Standard lithographic techniques were used to produce a mold from a silicon master spin-coated with SU-8 photoresist (MicroChem Corp.). PDMS chips were produced from this mold using Sylgard 184 Elastomer Kit (Dow Corning Corporation). Inlet and outlet holes were punched through PDMS using a pin vise (Technical Innovations, Inc.). PDMS and glass were activated by air plasma (Plasma Cleaner, Harrick Plasma) and bonded together to enclose the channels.

Beads and Dyes Suspensions. Fluorescent monodisperse (10 μm, 1.05 g/mL) and nonfluorescent polydisperse particles (11 μm, 1.05 g/mL) were purchased from Duke Scientific. Particles were mixed to the desired length fraction by dilution in deionized water, from $\varphi = 0$ to 55%, for wt/vol % varying between 0.1% and 2.5%. To help visualization, the fluid stream can be mixed with fluorescein (1 mM in deionized water) or with blue food dye. Particle suspensions were pumped into the devices through Polyether ether ketone tubing (Upchurch Scientific Product No. 1569) using a syringe pump (Harvard Apparatus PHD 2000), for flow rates ranging from 5 to 300 μL/min.

Cell Suspensions and Blood. HeLa cells cultured in RPMI medium 1640 with 10% FBS were trypsinized and resuspended in Phosphate Buffered Saline (PBS) before use, to achieve $\varphi = 4\%, 25\%$, and 33% assuming an average diameter of 15 μm. Blood was collected from healthy volunteers in BD Vacutainer tubes by a trained phlebotomist and diluted with PBS with various factors of dilution (50X, 20X, and 10X). To facilitate white blood cell extraction, red cells were selectively lysed (eBiosciences, 1X RBC Lysis Buffer) and removed after serial centrifugations. White blood cells were resuspended in PBS before use, to $\varphi = 35\%$ assuming an average diameter of 12 μm.

Imaging and Transfer Characterization. Fluorescent images were recorded using a Photometrics CoolSNAP HQ2 CCD camera mounted on a Nikon Eclipse Ti microscope. Images were captured with Nikon NIS-Elements AR 3.0 software. Based on these images, the intensity profile of a given channel cross-section can be drawn. The corresponding extent of transverse transport is characterized by transport factor (TF), defined as $2 \times (\Delta H/w - 0.5)$, with $\Delta H/w$ the extent of the channel cross-section whose intensity is greater than critical intensity ($I_c = 0.2(I_{\max} - I_{\min}) + I_{\min}$) (Fig. S6). Based on the cross-sectional intensity profile, transport factor (TF) is calculated, which ranges from 0 to 1 where 0 and 1, respectively, correspond to zero and full transfer (homogenous distribution of the fluorescent dye on the cross-section of the channel). Confocal imaging was performed at the California NanoSystems Institute (CNSI) using a Leica inverted SP1 confocal microscope. Confocal images are the average of eight y-z scans. For high-precision observations and measurements, some sequences were also recorded using a Phantom v7.3 high-speed camera (Vision Research Inc.) and Phantom Camera Control software.

Integration of Fluid Switching and Mixing Around Beads and Cells. Particle/cell suspensions were coflowed with a PBS washing buffer labeled with 250 μM fluorescein, respectively, at the Q_P and Q_B flow rates. L cm downstream, particle-/cell-containing solution was collected in one of two or more outlets configured to take only a subfraction of the total liquid flow. The subfraction of solution without particles was also obtained (Fig. S10*A*). For each outlet and each flow rate, fluorescence intensity is measured with a plate reader (Tecan) and converted to an exchange percentage (exchange %) defined by a calibration curve obtained with serial dilutions of the fluorescent washing buffer. This parameter represents the proportion of fluorescent buffer stream transferred into the particle-laden collected fraction. Similarly, we define the contamination % as the concentration of particles contaminating the buffer outlet compared to the initial concentration of the particle suspension.

1. Di Carlo D, Irimia D, Tompkins RG, Toner M (2007) Continuous inertial focusing, ordering, and separation of particles in microchannels. *Proc Natl Acad Sci USA* 104:18892–18897.
2. Humphry KJ, Kulkarni PM, Weitz DA, Morris JF, Stone HA (2010) Axial and lateral particle ordering in finite Reynolds number channel flows. *Phys Fluids* 22:081703.
3. Matas JP, Glezer V, Guazzelli E, Morris JF (2004) Trains of particles in finite-Reynolds-number pipe flow. *Phys Fluids* 16:4192.
4. Hur SC, Tse HTK, Di Carlo D (2010) Sheathless inertial cell ordering for extreme throughput flow cytometry. *Lab Chip* 10:274–280.
5. Lee W, Amini H, Stone HA, Di Carlo D (2010) Microfluidic crystals: Self-assembly and control of particle streams. *Proc Natl Acad Sci* 107:22413–22418.
6. Di Carlo D (2009) Inertial microfluidics. *Lab Chip* 9:3038–3046.

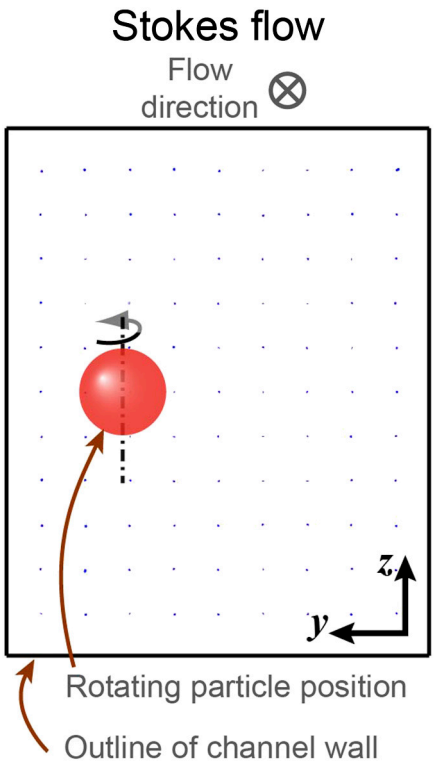

Fig. S1. Net lateral velocity field in Stokes flow. Due to the symmetry of the system lack of inertia (i.e., $\rho = 0$), the net transverse transfer for all points across the channel is equal to zero within numerical accuracy.

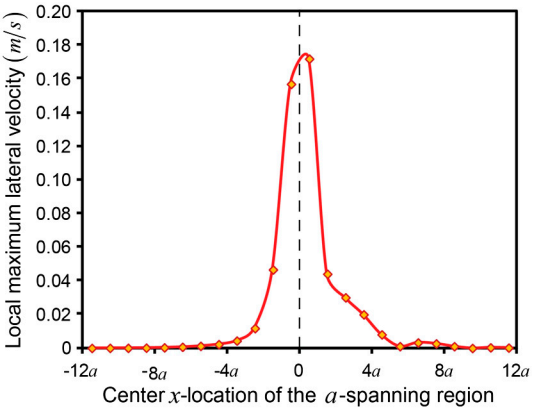

Fig. S2. Local net lateral motion of the fluid in channel subregions. The vertical axis represents the local V_{max} in channel subregions and the horizontal axis shows the x position of an integrated subregion of the channel relative to the x position of the particle center. Each subregion contains a portion of the channel length that spans a distance a. This shows that most of the lateral motion occurs near the particle and a distance of 10a up- and downstream of the particle captures the majority of the fluid lateral motion. The amount of lateral motion outside of this region is smaller than our numerical precision. The length of this region could vary for different flow conditions (for instance, it becomes larger for higher flow rates). We investigate each flow condition prior to applying our analysis method for each case.

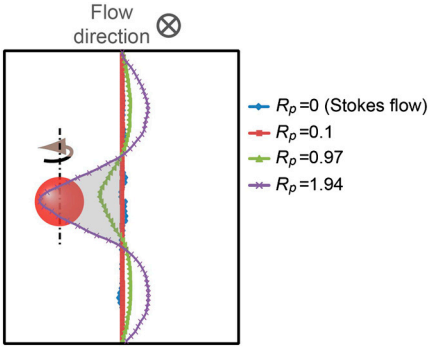

Fig. S3. Net y direction mass transfer for different particle Reynolds numbers. Whereas even at high flow rates, no net transfer is observed in the Stokes flow simulation (blue, corresponding to $Q = 200$ μL/min), the transfer in inertial flow is strongly amplified with increasing R_p.

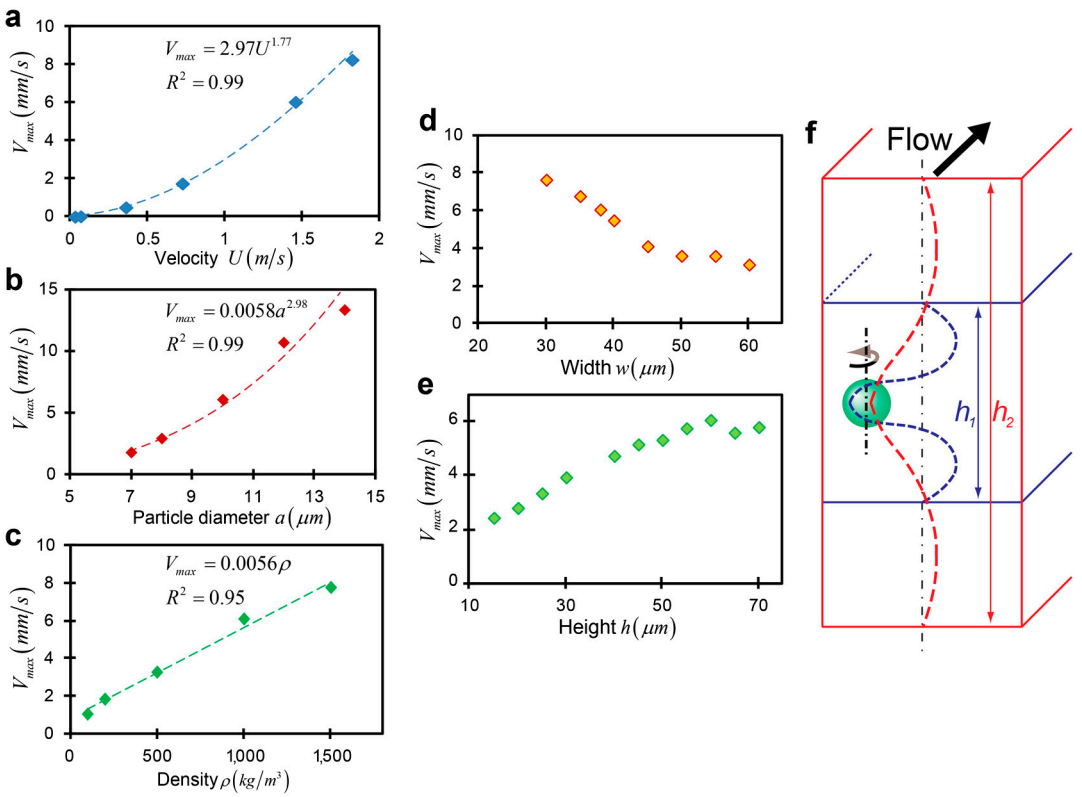

Fig. S4. Scaling of the transverse transport velocity (V_{max}) with dimensional parameters and a schematic of transport for different channel heights. Particles are simulated occupying inertial focusing positions along the channel width. Except for one variable in each graph, the system parameters are as follows: $w = 38$ μm, $h = 60$ μm, $a = 10$ μm, $Q = 200$ μL/ min, $\rho = 1{,}000$ kg/m^3, $\mu = 0.001$ Pa.s, and the particle is laterally located at its focusing position. (*A*) Transverse velocity has a best fit with $U^{1.77}$. This scaling is consistent with the importance of the inertia of the fluid around the particle. (*B*) There is a significant dependence on particle size, approximately a^3. The strong effect of the particle size is consistent with the amount of fluid transferred around the particle scaling with particle volume. (*C*) The relation between the transport and the density appears linear. (*D*) With increasing width and a channel height of 60 μm, the transfer decreases until it saturates for low aspect ratio channels. (*E*) With increasing height at a fixed channel width of 38 μm, the transfer increases until it saturates for high aspect ratios. (*F*) These results are consistent with the argument that when the system has a short height (h_1) compared to width it is constrained to have return flows, satisfying conservation of mass in close proximity to the generating flow around the particle. Thus, the return flow compresses the generating flow and eliminates a portion of the potential transfer. However, for taller heights (h_2), the return flows are able to extend in the z direction, allowing for full transfer to occur. Note that confinement in the velocity gradient direction (width) leads to a stronger effect than channel height (V_{max} varies by a factor of 3 compared to 1.5 for a twofold change in dimension).

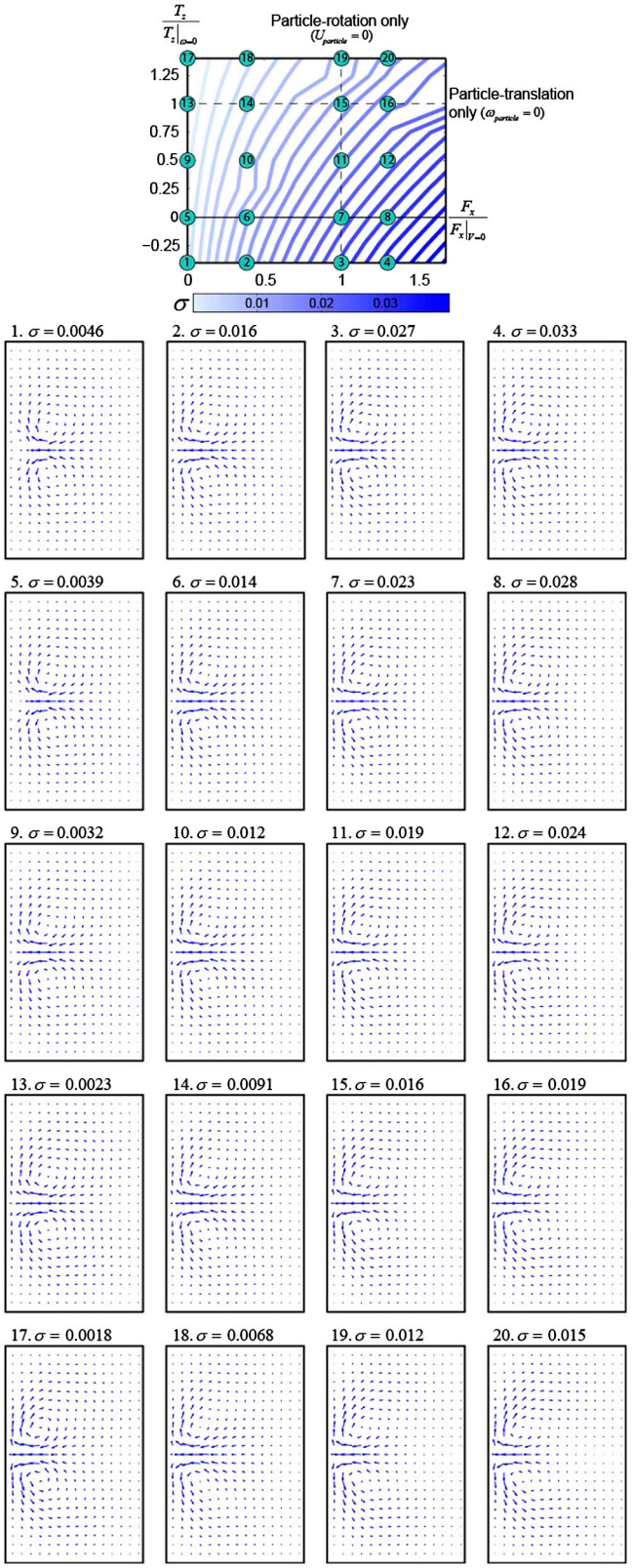

Fig. S5. Transverse transport velocity for various physical constraints on the particle. In order to obtain a better understanding of how different components of particle motion contribute to the transport, we numerically solved for different conditions of predefined drag and torque on the particle. The results show that the velocity difference between the particle and the fluid and also particle rotation contribute to increased transport, with the former being the more significant factor. While the overall shape of the net secondary flow in the channel is quite similar for different drag and torque imposed on the particle, the intensity of the flow is heavily influenced by them. For instance, σ in the case of a overrotating, backward-moving particle (case 4) is nearly 20 times larger than a counter-rotating particle moving faster than the background flow (case 17). These results also suggest that translational slip has a more significant effect on the secondary flow, compared to rotational slip.

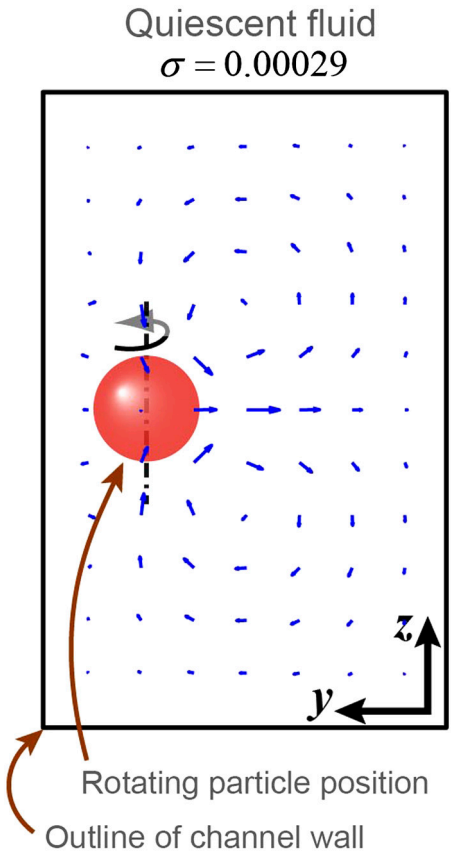

Fig. S6. Numerical simulations indicate that a rotating particle in quiescent fluid located in a channel also creates a net secondary flow. The direction of this flow is opposite to a particle similarly positioned in the presence of a bulk channel flow, and it is much weaker in magnitude. Although there is no downstream flow (thus $U_{avg} = 0$), we obtain a normalized transport, σ, by dividing by U_{avg} that yields the same torque-free rotation rate imposed on the particle in the current simulation.

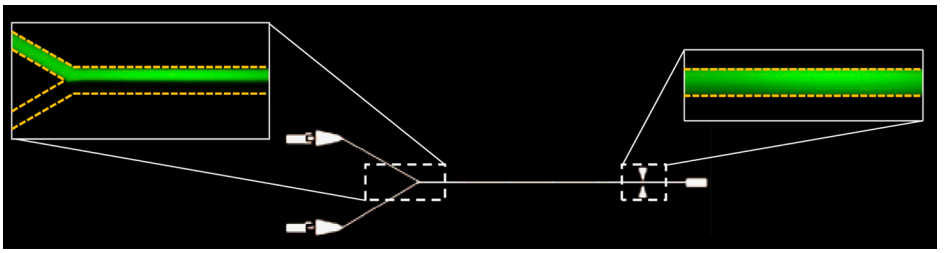

Fig. S7. Experimental device. A drawing of the mask used to make the device is shown. Example fluorescent images captured at the junction and 2.5 cm downstream are shown for reference. Only one inlet contains fluorescent dye, whereas the other solution is nonfluorescent.

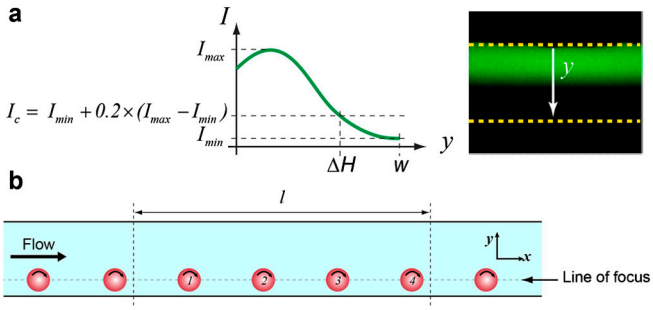

Fig. S8. Definition of transport factor (*TF*) and length fraction (φ). (*A*) The intensity profile at the point of interest along the channel is first extracted. Critical intensity is calculated as $I_c = 0.2(I_{\max} - I_{\min}) + I_{\min}$ and then used to define *TF* as $2 \times (\Delta H/w - 0.5)$, with $\Delta H/w$ being the extent of the channel cross-section in which the intensity is greater than I_c. (*B*) Length fraction φ is essentially a measure of particle concentration in the channel. It is defined as the fraction of the channel length that is occupied by particles, assuming that all particles are focused to a single stream. Equivalently, $\varphi = \sum a_i/l$. It is preferred to represent the concentration of the particles in channel flow as length fraction, rather than the conventional volumetric concentration V_f, because it provides a more comprehensive description of how many particles are positioned to disturb the flow. This parameter is more relevant than the volume fraction because, for the cases tested, particles over the whole channel volume are focused to a single focal stream. Therefore, increasing the channel dimensions while maintaining the same volume fraction is expected to counterintuitively lead to different transport rates as the increased number of particles from the increased channel volume are focused to the same stream. The relationship between length fraction and volume fraction is $\varphi = 6whV_f/\pi a^2$. Note that due to the relative lengths of the system, a large φ might correspond to a moderate V_f. For instance, $\varphi = 25\%$ in our channels ($w_{\text{stream}} = 19$ μm, $h = 60$ μm, $a = 10$ μm) corresponds to $V_f = 1.148\%$.

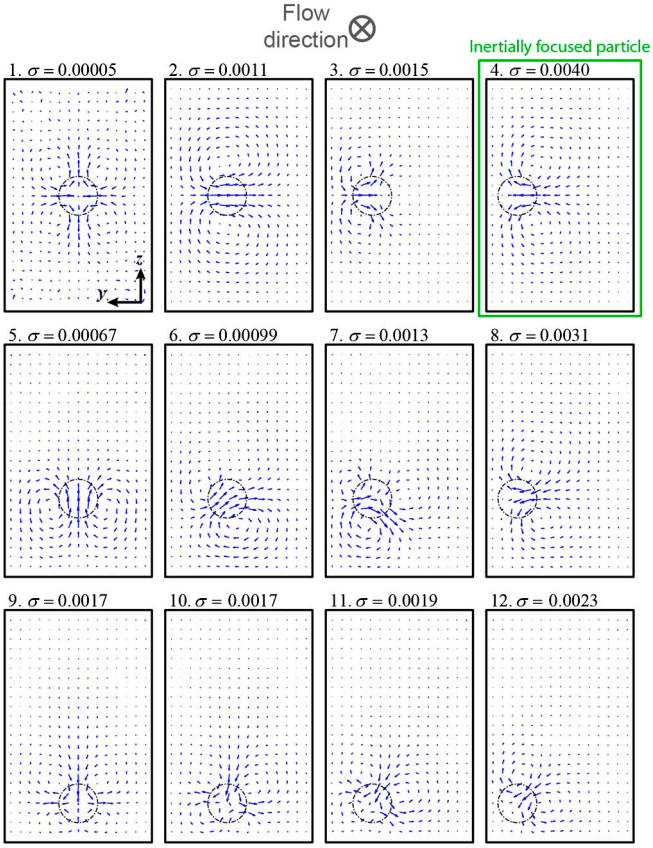

Fig. S9. The cross-sectional position of the drag- and torque-free particle in the channel affects the secondary flow created. A slight change in the position of the particle from its focusing position in the *y* direction results in full reversal of the secondary flow (compare cases 3 and 4). Displacement in the *z* direction creates additional complexity in the shape and direction of the secondary flows. For instance, three secondary flows exist in case 7. This shows that even when the particles are flowing on the same half of the channel, the secondary flows they induce might not be in-phase and that slight displacement of the particle from its focusing position might result in a set of secondary flows that are deconstructive (compared to inertially focused particles).

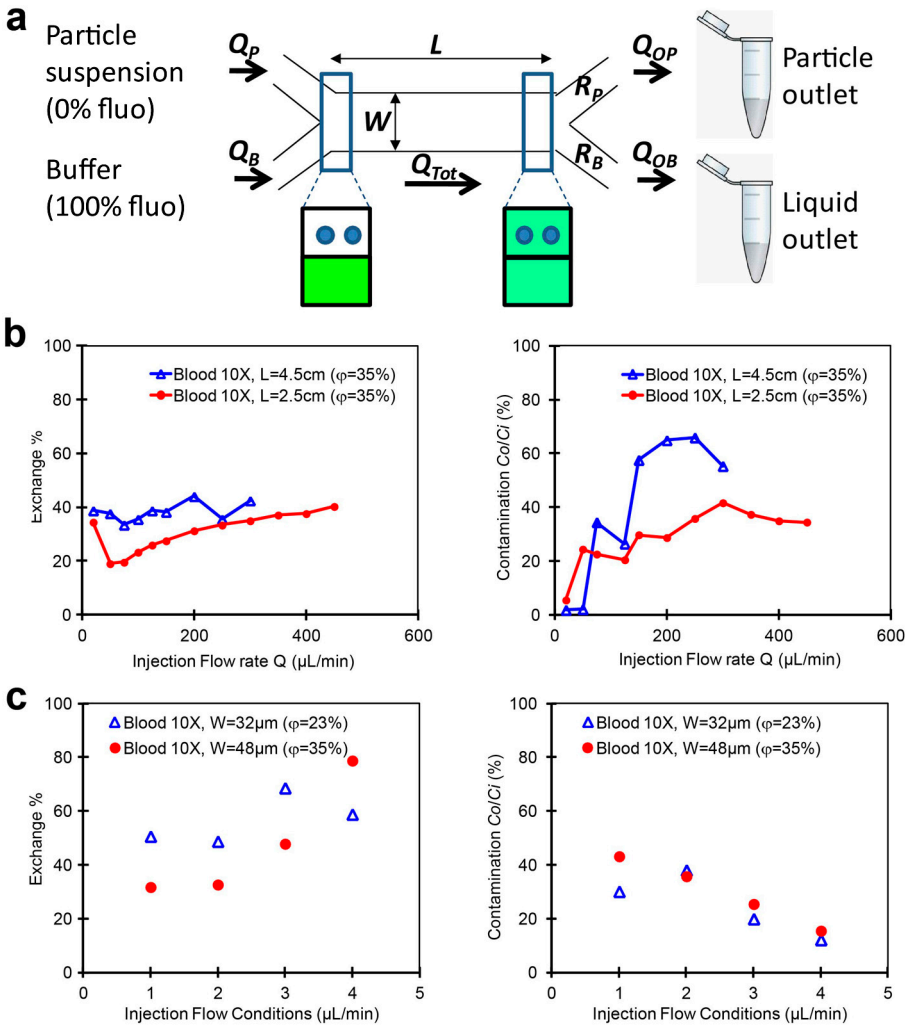

Fig. S10. Integration of fluid exchange or mixing around beads and cells in a microfluidic platform. (*A*) Schematic of the two-inlet/two-outlet device used for exchange and mixing experiments. Bead or cell suspensions are coflowed with a washing buffer stream containing dyes, respectively, at the Q_P and Q_B flow rates. *L* cm downstream, the two streams are extracted in two separate outlets and the exchange of fluid surrounding the particle stream is characterized for each outlet and each flow rate. The fluorescence intensity measured with a plate reader is converted to an exchange percentage (exchange %) defined based on a calibration curve. Once again, the simplicity of the device is a key feature. (*B*) Representation of exchange % and contamination for 10X-diluted ($\varphi = 35\%$) blood injected in two channel lengths, 2.5 and 4.5 cm, with $w = 48$ μm. A transfer of fluid around the blood cells is observed (exchange % up to 40% at higher flow rates). However, a significant contamination of the wash stream with red blood cells is measured for both channel lengths (>40%). Still longer channels lead to higher contamination, because red blood cells have more time to migrate across the channel. Such results demonstrate an efficient mixing function, i.e., the transfer of fluid around the blood cells but also the migration of concentrated red cells in all channel widths. (*C*) Representation of exchange % and contamination for 10X-diluted blood injected in two channel widths, 32 μm ($\varphi = 23\%$) and 48 μm ($\varphi = 35\%$), with $L = 2.5$ cm. As observed for Flow Conditions 1 and 2 (equal inlet flow rates, $Q_P = Q_B = 100$ and 150 μL/ min for $w = 32$ μm, $Q_P = Q_B = 150$ and 200 μL/ min for $w = 48$ μm), the channel width significantly affects the amount of transfer because a narrower channel means a higher R_p, thus more fluid transfer, while contamination remains the same. To simultaneously increase the amount of fluid transferred in the cell stream and reduce contamination of cells in the buffer stream, the ratio of inlet flow rates can be adjusted with the cell stream being thinner than the liquid stream, such as for Flow Conditions 3 and 4 (different inlet flow rates, $Q_P = 80/Q_B = 120$ μL/ min and $Q_P = 100/Q_B = 200$ μL/ min for $w = 32$ μm, $Q_P = 100/Q_B = 200$ μL/ min and $Q_P = 100/Q_B = 300$ μL/ min for $w = 48$ μm).

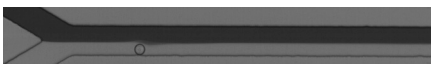

Movie S1. Demonstration of particle-induced convection at intermediate flow rate. The PDMS particles of up to 50 μm in size are flowing in a 122×70 μm channel at 54 μL/ min and food dye (injected from the top inlet) is dragged by the rotating particle towards the bottom of the channel. As a result, the lateral convection dominates lateral diffusion. The disturbance flow is clearly visible for large particles. It is also evident that, as for instance seen in Movie S4, the effect is diminished for smaller particles.

Movie S1 (AVI)

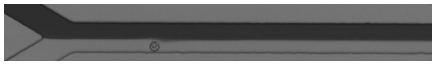

Movie S2. Demonstration of particle-induced convection at intermediate flow rate. The PDMS particles of up to 50 μm in size are flowing in a 122 × 70 μm channel at 54 μL/ min and food dye (injected from the top inlet) is dragged by the rotating particle towards the bottom of the channel. As a result, the lateral convection dominates lateral diffusion. The disturbance flow is clearly visible for large particles. It is also evident that, as for instance seen in Movie S4, the effect is diminished for smaller particles.

Movie S2 (AVI)

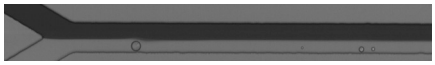

Movie S3. Demonstration of particle-induced convection at intermediate flow rate. The PDMS particles of up to 50 μm in size are flowing in a 122 × 70 μm channel at 54 μL/ min and food dye (injected from the top inlet) is dragged by the rotating particle towards the bottom of the channel. As a result, the lateral convection dominates lateral diffusion. The disturbance flow is clearly visible for large particles. It is also evident that, as for instance seen in Movie S4, the effect is diminished for smaller particles.

Movie S3 (AVI)

Movie S4. Demonstration of particle-induced convection at intermediate flow rate. The PDMS particles of up to 50 μm in size are flowing in a 122 × 70 μm channel at 54 μL/ min and food dye (injected from the top inlet) is dragged by the rotating particle towards the bottom of the channel. As a result, the lateral convection dominates lateral diffusion. The disturbance flow is clearly visible for large particles. It is also evident that, as for instance seen in Movie S4, the effect is diminished for smaller particles.

Movie S4 (AVI)

Movie S5. Demonstration of particle-induced convection at intermediate flow rate. The PDMS particles of up to 50 μm in size are flowing in a 122 × 70 μm channel at 54 μL/ min and food dye (injected from the top inlet) is dragged by the rotating particle towards the bottom of the channel. As a result, the lateral convection dominates lateral diffusion. The disturbance flow is clearly visible for large particles. It is also evident that, as for instance seen in Movie S4, the effect is diminished for smaller particles.

Movie S5 (AVI)